Medical Image Analysis 31 (2016) 63–76

Contents lists available at ScienceDirect

Medical Image Analysis

journal homepage: www.elsevier.com/locate/media

A benchmark for comparison of dental radiography analysis algorithms☆

Ching-Wei Wang[a,b,*], Cheng-Ta Huang[a,b], Jia-Hong Lee[a,b], Chung-Hsing Li[c,d], Sheng-Wei Chang[c], Ming-Jhih Siao[c], Tat-Ming Lai[e], Bulat Ibragimov[f], Tomaž Vrtovec[f], Olaf Ronneberger[g], Philipp Fischer[g], Tim F. Cootes[h], Claudia Lindner[h]

[a] Graduate Institute of Biomedical Engineering, National Taiwan University of Science and Technology, Taiwan
[b] NTUST Center of Computer Vision and Medical Imaging, Taiwan
[c] Orthodontics and Pediatric Dentistry Division, Dental Department, Tri-Service General Hospital, Taiwan
[d] School of Dentistry and Graduate Institute of Dental Science, National Defense Medical Center, Taipei, Taiwan
[e] Department of Dentistry, Cardinal Tien Hospital, Taipei, Taiwan
[f] Faculty of Electrical Engineering, University of Ljubljana, Tržaška 25, SI-1000 Ljubljana, Slovenia
[g] University of Freiburg, Germany
[h] Centre for Imaging Sciences, The University of Manchester, UK

ARTICLE INFO

Article history:
Received 8 September 2015
Revised 2 February 2016
Accepted 19 February 2016
Available online 28 February 2016

Keywords:
Cephalometric tracing
Anatomical segmentation and classification
Bitewing radiography analysis
Challenge and benchmark

ABSTRACT

Dental radiography plays an important role in clinical diagnosis, treatment and surgery. In recent years, efforts have been made on developing computerized dental X-ray image analysis systems for clinical usages. A novel framework for objective evaluation of automatic dental radiography analysis algorithms has been established under the auspices of the IEEE International Symposium on Biomedical Imaging 2015 Bitewing Radiography Caries Detection Challenge and Cephalometric X-ray Image Analysis Challenge. In this article, we present the datasets, methods and results of the challenge and lay down the principles for future uses of this benchmark. The main contributions of the challenge include the creation of the dental anatomy data repository of bitewing radiographs, the creation of the anatomical abnormality classification data repository of cephalometric radiographs, and the definition of objective quantitative evaluation for comparison and ranking of the algorithms. With this benchmark, seven automatic methods for analysing cephalometric X-ray image and two automatic methods for detecting bitewing radiography caries have been compared, and detailed quantitative evaluation results are presented in this paper. Based on the quantitative evaluation results, we believe automatic dental radiography analysis is still a challenging and unsolved problem. The datasets and the evaluation software will be made available to the research community, further encouraging future developments in this field. (http://www-o.ntust.edu.tw/~cweiwang/ISBI2015/)

1. Introduction

Dental radiography analysis plays an important role in clinical diagnosis, treatment and surgery as radiographs can be used to find hidden dental structures, malignant or benign masses, bone loss and cavities. During diagnosis and treatment procedures such as root canal treatment, caries diagnosis, diagnosis and treatment planning of orthodontic patients, dental radiography analysis is mandatory. Dental X-ray images can be categorized into two types, i.e. the intraoral ones and the extraoral ones (Kumar, 2011). The intraoral radiographs include the bite wing X-ray images to present the details of the upper and lower teeth in an area of the mouth, the periapical X ray images to monitor the whole tooth and the occlusal X-ray image to track the development and placement of an entire arch of teeth in either the upper or lower jaw. On the other hand, the extraoral radiographs are used to detect dental problems in the jaw and skull, such as the cephalometric projections and the panoramic X-ray images.

Cephalometric analysis describes the interpretation of patients' bony, dental and soft tissue structures and provides all images for the orthodontic analysis and treatment planning. However, in clinical practice, manual tracing of anatomical structures (as shown

☆ "This paper was recommended for publication by James Duncan".

* Corresponding author at: Graduate Institute of Biomedical Engineering, National Taiwan University of Science and Technology, Taiwan. Tel.: +886 2 27303749; fax: +886 2 27303733.
E-mail address: cweiwang@mail.ntust.edu.tw (C.-W. Wang).

http://dx.doi.org/10.1016/j.media.2016.02.004

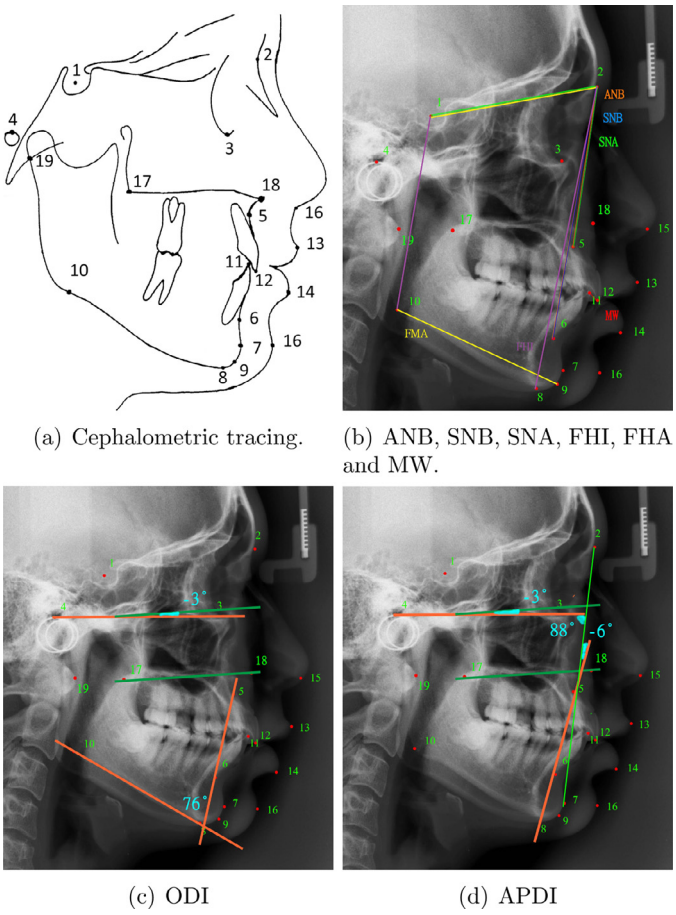

(a) Cephalometric tracing. (b) ANB, SNB, SNA, FHI, FHA and MW.

(c) ODI (d) APDI

Fig. 1. (a) Cephalometric tracing (b–d) clinical measurements for classification of anatomical abnormalities: ANB = $\angle L_5L_2L_6$; SNB = $\angle L_1L_2L_6$; SNA=$\angle L_1L_2L_5$; FHI = $\overline{L_1L_{10}}/\overline{L_2L_8}$; FHA=$\angle L_1L_2L_{10}L_9$; MW=$|\overline{L_{12}L_{11}}|$ where $x(L_{12}) > x(L_{11})$, otherwise, MW=$-|\overline{L_{12}L_{11}}|$; ODI=$\angle L_5L_6L_8L_{10} + \overline{L_{17}L_{18}L_4L_3}$, in this example, the ODI is $(76^\circ + (-3^\circ) = 73^\circ)$, in the normal range with a slight tendency to be an openbite; APDI = $\overline{L_3L_4L_2L_7} + \overline{L_2L_7L_5L_6} + \overline{L_4L_3L_{17}L_{18}}$, in this example, the APDI is $(88^\circ + (-6^\circ) + (-3^\circ) = 79^\circ)$, which falls within the normal range. .

in Fig. 1) is commonly conducted during treatment planning. This procedure is time consuming and subjective. Automated landmark detection for diagnosis and orthodontic treatment of cephalometry could be the solution to facilitate these issues. However, automated landmark detection with high precision and success rate is challenging. In recent years, efforts have been made to develop computerized dental X-ray image analysis systems for clinical usages, such as in anatomical landmark identification (Nikneshan, 2015; Zhou and Abdel-Mottaleb, 2005), image segmentation (Lai and Lin, 2008; Rad, 2013), diagnosis and treatment (Lpez-Lpez, 2012; Nakamoto, 2008; Wriedt, 2012). In 2014, we held an automatic cephalometric X-ray landmark detection challenge at IEEE ISBI 2014 with 300 cephalometric X-ray images, and the best overall detection rate for 19 anatomical landmarks was 71.48% with an accuracy of within 2mm. The 2014 challenge outcomes indicate that automatic cephalometric X-ray landmark detection is still an unsolved problem. Hence, the first part of this study is to investigate suitable automated methods in cephalometric X-ray landmark detection. In this study, a larger clinical database was built using data from 400 patients.

Furthermore, apart from anatomical landmark detection in cephalometric images, a new classification task for the clinical diagnosis of anatomical abnormalities using these landmarks was added in this study. In order to be critical and descriptive in clinical practice, it is more useful to analyse angles and linear measurements rather than just point positions. Many classification methods have been proposed for cephalometric analysis, such as Ricketts analysis (Ricketts, 1982), Downs analysis (Downs, 1948), Tweed analysis (Tweed, 1954), Sassouni analysis (Sassouni, 1955) and Steiner analysis (Steiner, 1953). Therefore, the second part of this study was to automatically classify patients into different anatomical types to infer a clinical diagnosis.

Apart from the cephalometric analysis, caries detection and dental anatomy analysis are important in clinical diagnosis and treatment. Dental caries is a transmissible bacterial disease of the teeth that would destructs the structure of teeth, and the dentist has approached diagnosing and treating dental caries based mostly on radiographs. While dental caries is a disease process, the term is routinely used to describe radiographic radiolucencies.

Radiographic examination can improve the detection and diagnosis of the dental caries. In the clinical practice, caries lesions have traditionally been diagnosed by visual inspection in combination with radiography. Therefore, automated caries detection systems with high reproducibility and accuracy would be welcomed in clinicians' search for more objective caries diagnostic methods (Wenzel, 2001, 2002). Several research studies focused on pattern recognition or segmentation of dental structures, such as in caries detection (Huh, 2015; Oliveira and Proenc, 2011), root canal edge extraction (Gayathri and Menon, 2014), identity matching (Jain and Chen, 2004; Zhou and Abdel-Mottaleb, 2005) and teeth classification (Lin, 2010). Automated caries lesion detection technologies provide potential diagnostic data for dental practitioners and assist identifying signs of various diseases. However, accurate and objective methods for radiographic caries diagnosis are poorly explored. Therefore, the third part of this study was to investigate possible automated methods both for detection of caries and for dental anatomy analysis in bitewing radiographs.

This paper presents the evaluation and comparison of a representative selection of current methods presented during the Grand Challenges in Dental X-ray Image Analysis held in conjunction and with the support of the IEEE ISBI 2015. There are two main challenges, the *Automated Detection and Analysis for Diagnosis in Cephalometric X-ray Image* and the *Computer-Automated Detection of Caries in Bitewing Radiography*, and the first challenge contains two challenge tasks: (i) to identify anatomical landmarks on lateral cephalograms, and (ii) to classify anatomical types based on the anatomical landmarks. Only the first task of the first challenge of this study is similar to a related challenge held at 2014 IEEE ISBI challenge. The second challenge- *Computer-Automated Detection of Caries in Bitewing Radiography* and the second challenge task of Challenge 1 - classifying anatomical types based on the anatomical landmarks are both completely new. In addition, for the first challenge, the dataset was enlarged to now include 400 patients. In comparison to the challenge held at IEEE ISBI 2014, this study includes a new challenge, new data and a new challenge task (see Table 1). The outline of the paper is organized as follows. In Section 2, the challenge aims, participants, image datasets and evaluation approaches are described. The methodologies and detailed quantitative evaluation results of *Challenge 1* and *Challenge 2* are presented in Sections 3 **and** 4, respectively. Finally, conclusions are given in Section 5**.**

2. Grand challenges in dental X-ray image analysis

2.1. Organization

The goals of this grand challenge are to investigate automatic methods for *Challenge 1-1*: identifying anatomical landmarks on lateral cephalograms, *Challenge 1-2*: classifying anatomical types based on the anatomical landmarks, and *Challenge 2*: segmenting seven tooth structures on bitewing radiographs. The 19 anatomical

Table 1
The tasks and datasets of the IEEE ISBI 2014 and the IEEE ISBI 2015 challenges.

2014 - Landmark detection	2015 - Landmark detection, pathology classification and teeth segmentation
• Landmark detection in cephalometric radiographs	• Challenge 1: Automated detection and analysis for diagnosis in cephalometric x-ray image • Task1: landmark detection (similar to 2014) • Task2: classification of anatomical types (New) • Challenge 2: computer-automated detection of caries in bitewing radiography (new) • Task 1: segmentation of seven tooth structures (new)
Common task between 2014/2015: landmark detection in cephalometric radiographs	
Data	
• 300 cephalometric radiographs	• 400 cephalometric radiographs (100 additional patients) • 120 bitewing radiographs (new)

Table 2
Eight standard clinical measurement methods for classification of anatomical types.

Method	(1) ANB	(2) SNB	(3) SNA	(4) ODI	(5) APDI	(6) FHI	(7) FHA	(8) MW
Type 1	3.2° ~ 5.7° Class I (normal)	74.6° ~ 78.7° Normal mandible	79.4° ~ 83.2° Normal maxilla	Normal: 74.5° ± 6.07°	Normal: 81.4° ± 3.8°	Normal: 0.65 ~0.75	Normal: 26.8° ~ 31.4°	Type 1: Normal: 2 mm ~ 4.5 mm
Type 2	>5.7° Class II	<74.6° Retrognathic mandible	>83.2° Prognathic maxilla	>80.5° Deep bite tendency	<77.6° Class II tendency	>0.75 Short face tendency	>31.4° Mandible high angle tendency	Type 2: MW = 0 mm Edge to edge Type 3: MW <0 mm Anterior cross bite
Type 3	<3.2° Class III	>78.7° Prognathic mandible	<79.4° Retrognathic maxilla	<68.4° Open bite tendency	>85.2° Class III tendency	<0.65 Long face tendency	<26.8° Mandible lower angle tendency	Type 4: MW >4.5 mm Large over jet

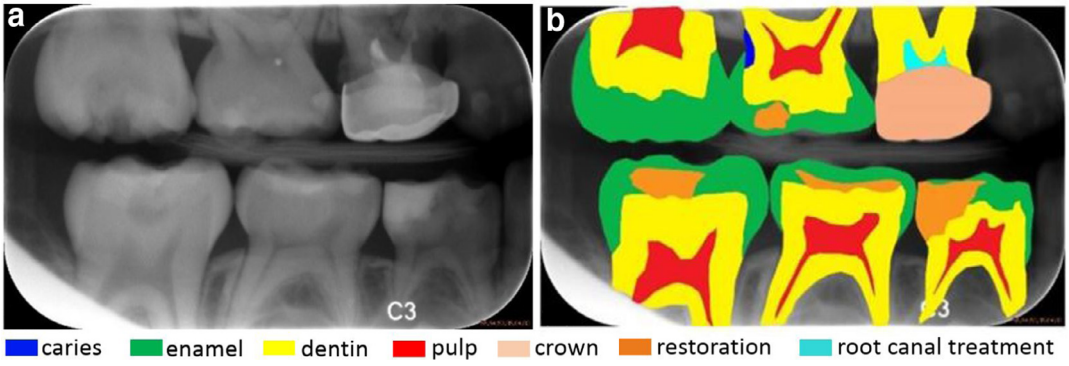

Fig. 2. Bitewing radiographs: (a) a raw image with (b) seven dental structures highlighted, including (1) caries with blue color, (2) enamel with green color, (3) dentin with yellow color, (4) pulp with red color, (5) crown with skin color, (6) restoration with orange color and (7) root canal treatment with cyan color. The images are captured using the SOREDEX system (SOREDEX, Finland), that is devised with an optional image plate identification system (IDOT) for quality control, and 'C3' on the image indicates the active/frontal side in the IDOT system.

landmarks to be detected on lateral cephalograms are the sella, the nasion, the orbitale, the porion, the subspinale (A point), the supramentale (B point), the pogonion, the menton, the gnathion, the gonion, the lower incisal incision, the upper incisal incision, the upper lip, the lower lip, the subnasal, the soft tissue pogonion, the posterior nasal spine, the anterior nasal spine, the anterior nasal spine and the articulare as shown in Fig. 1(a). For the classification of anatomical types based on the obtained anatomical landmarks, eight standard clinical measurement methods (Downs, 1948; Kim, 1974; Kim and Vietas, 1978; McNamara, 1984; Nanda and Nanda, 1969; Steiner, 1953; Tweed, 1946) were included as shown in Table 2 and illustrated in Fig. 1(b)–(d). For the analysis of the dental anatomy of bitewing radiographs, seven tooth structures were included: caries, enamel, dentin, pulp, crown, restoration, and root canal treatment (see Fig. 2).

There were two stages in both challenges. In stage 1, a training dataset and a first test dataset were released for method development. In stage 2, an on-site competition was organized for which a second test dataset was used. The results of all individual methods were compared to the ground truth data, and extensive quantitative evaluation was performed to assess the performance of all methods.

2.2. Participants

A total of 18 teams (from 12 countries) registered for the 2015 IEEE ISBI grand challenge, and the four teams listed below were accepted in stage 1 and invited to the on-site competition in stage 2. The four approaches are described in Sections 3.1 and 4.1, respectively. In landmark detection of cephalometric radiographs, we also compare five methods submitted to the 2014 ISBI challenge, and details of the five methods can be referred to (Wang, 2015).

(1) Ibragimov et al., computerized cephalometry by game theory with shape- and appearance-based landmark refinement (Slovenia).

Table 3
Image distribution in the training, Test1 and Test2 data.

	Challenge 1: cephalometric radiographs		Challenge 2: bitewing radiographs
	2014	2015	2015
Training	100	150	40[a]
Test1	100	150	40[a]
Test2 (on-site competition)	100	100[a]	40[a]

[a] The new data collected in 2015.

(2) Lindner and Cootes, fully automatic cephalometric evaluation using random forest regression-voting (UK).
(3) Lee et al., dental X-ray image segmentation using random forest (Taiwan).
(4) Ronneberger et al., dental X-ray image segmentation using a U-shaped deep convolutional network (Germany).

2.3. Datasets

400 cephalometric radiographs were collected from 400 patients aged six to 60 years. The cephalograms were acquired in TIFF format with Soredex CRANEXr Excel Ceph machine (Tuusula, Finland) and Soredex SorCom software (3.1.5, version 2.0), and the image resolution was 1935 × 2400 pixels. For evaluation, 19 landmarks were manually marked in each image and reviewed by two experienced medical doctors; the ground truth is the average of the markups by both doctors. For the classifications of anatomical types, eight clinical measurement methods were used (see illustrations in Fig. 1 and classifications in Table 2):

1. ANB $= \angle L_5L_2L_6$, the angle between the landmark 5, 2 and 6
2. SNB $= \angle L_1L_2L_6$;
3. SNA $= \angle L_1L_2L_5$
4. ODI $= \angle\overline{L_5L_6}\overline{L_8L_{10}} + \overline{L_{17}L_{18}}\overline{L_4L_3}$, the arithmetic sum of the angle between the AB plane ($\overline{L_5L_6}$) to the Mandibular Plane (MP, $\overline{L_8L_{10}}$)and the angle of the Palatal Plane (PP, $\overline{L_{17}L_{18}}$) to Frankfort Horizontal plane (FH, $\overline{L_4L_3}$)
5. APDI $= \overline{L_3L_4}\overline{L_2L_7} + \overline{L_2L_7}\overline{L_5L_6} + \overline{L_3L_4}\overline{L_{17}L_{18}}$
6. FHI $= \overline{L_1L_{10}}/\overline{L_2L_8}$, the ratio of the Posterior Face Height (PFH = the distance from L_1 to L_{10}) to the Anterior Face Height (AFH = the distance from L_2 to L_8)
7. FHA $= \angle\overline{L_1L_2}\overline{L_{10}L_9}$
8. MW $= |\overline{L_{12}L_{11}}|$ where $x(L_{12}) > x(L_{11})$, otherwise, MW $= -|\overline{L_{12}L_{11}}|$

For the bitewing radiography analysis, 120 images were collected from 120 patients, acquired in TIFF format with Sirona HELIODENT DS SIDEXIS machine (Salzburg, Austria) and EBM Viewer software (version 4.2c). For evaluation, seven types were manually marked in each image and reviewed by two experienced medical doctors.

Both datasets were randomly divided into three subsets as Training data, Test1 data and Test2 data for two stage testing (see Table 3). Ethical approval (IRB Number 1-102-05-017) was obtained to conduct the study by the research ethics committee of the Tri-Service General Hospital in Taipei, Taiwan. The datasets and the evaluation software will be made available to the research community, further encouraging future developments in this field. (http://www-o.ntust.edu.tw/~cweiwang/ISBI2015/).

2.4. Evaluation approaches

In cephalometric radiography analysis, three main criteria are used to evaluate the performance of the submitted methods.

- *Mean radial error*
  The radial error R is formulated as $R = \sqrt{\triangle x^2 + \triangle y^2}$, where $\triangle x$ is the absolute distance in the x-direction between the obtained landmark and the referenced landmark, and $\triangle y$ is the absolute distance in the y-direction between the obtained landmark and the referenced landmark. The mean radial error (MRE) and the associated standard deviation (SD) are defined as $MRE = \frac{\sum_{i=1}^{N} R_i}{N}$ and $SD = \sqrt{\frac{\sum_{i=1}^{N}(R_i - MRE)^2}{N-1}}$.
- *Success detection rate*
  For each landmark, medical doctors mark the location of a single pixel instead of an area as a referenced landmark location. If the absolute difference between the detected landmark and the referenced landmark is no greater than z mm, the detection of this landmark is considered as a successful detection; otherwise, it is considered as a misdetection. The success detection rate p_z with precision less than z mm is formulated as $p_z = \frac{\#\{j : \|L_d(j) - L_r(j)\| < z\}}{\#\Omega} \times 100\%$, where L_d, L_r represent the location of the detected landmark and the referenced landmark, respectively; z denotes four precision measurements used in the evaluation, including 2 mm, 2.5 mm, 3 mm and 4 mm; $j \in \Omega$, and $\#\Omega$ represents the number of detections made.
- *Confusion matrix and success classification rate*
  In the confusion matrix, each column of the matrix represents the instances of a predicted class, while each row represents the instances of the ground truth class. The averaged diagonal of a confusion matrix represents the success classification rate. Confusion matrices also provide valuable information on where misclassifications occur.

In bitewing radiography analysis, three main criteria are used to evaluate the performance of submitted methods, including *Sensitivity*= $\frac{TP}{TP+FN}$, *Specificity*= $\frac{TN}{TN+FP}$ and *F-score* = $\frac{2TP}{2TP+FP+FN}$, where *TP, TN, FP, FN* represent true positive, true negative, false positive and false negative, respectively.

3. Challenge 1: cephalometric radiography analysis

3.1. Methods

(1) *Ibragimov et al.*
Ibragimov et al. present a novel framework for landmark detection and skull morphology classification from cephalometric X-ray images. The appearance of landmarks is modeled by a random forest-based classifier with Haar-like appearance features (Ibragimov, 2015) computed from original scale and downscaled images, so that the global and local intensity appearance, respectively, are analyzed. To find optimal landmark positions in the target image, the statistic properties of the most representative spatial relationships among landmarks, defined by Gaussian kernel estimation and optimal assignment-based shape representation (Ibragimov, 2012), are computed. The agreement between the appearance and shape models corresponds to optimal landmark positions in the target image, and is found by applying game-theoretic optimization framework (Ibragimov, 2014). Additionally, each landmark is repositioned using random forest-based shape models considering positions of most reliable or the remaining landmarks in the system.

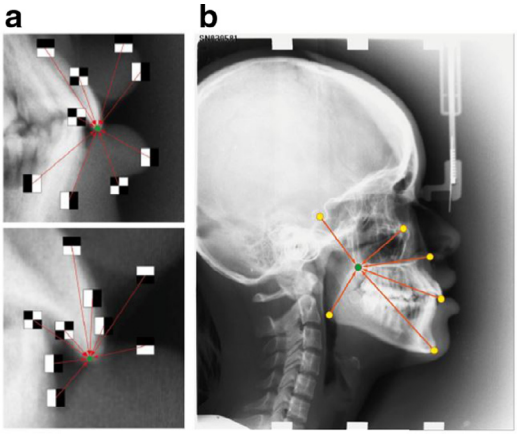

Fig. 3. (a) An illustration of the multi-scale appearance model that captures global appearance (top) and local appearance (bottom) of the target landmark (green circle). (b) An illustration of the shape model, where the position of the target landmark (green circle) is defined using the position of the remaining landmarks (yellow circles). (For interpretation of the references to color in this figure legend, the reader is referred to the web version of this article.)

Fig. 3 shows the illustrations of the multi-scale appearance model and the shape model.

(2) *Lindner and Cootes*

Recent work has shown that one of the most effective approaches to detect a set of landmark positions on an object of interest is to train Random Forests (RFs) to vote for the likely position of each landmark, then to find the shape model parameters which optimize the total votes over all landmark positions. Lindner and Cootes apply Random Forest regression-voting in the Constrained Local Model framework (RFRV-CLM) (Lindner, 2015) as part of a fully automatic landmark detection system (Lindner, 2013) to detect the 19 landmarks on new *unseen* images. In the RFRV-CLM approach, a RF is trained for each landmark to learn to predict the likely position of that landmark. During detection, a statistical shape model ((Cootes, 1995) is matched to the predictions over all landmark positions to ensure consistency across the set. A coarse-to-fine approach is used, and at each stage, the region around the current landmark position is mapped into a reference frame using a similarity transformation. For each of N landmarks we train a separate RF, which predicts the position of the landmark relative to an image patch. Each tree in the RF is trained on patches sampled at random displacements from the known position in the training set, and at each node a left/right split decision is made based on Haar-like features (Viola and Jones, 2001) from the patch. On a new image, the RF is scanned over a region around the current landmark position, and each tree in the RF votes for the likely new position. Votes are accumulated in a voting image $V_l()$ for landmark l (see Fig. 4). Lindner and Cootes then seek the model shape and pose parameters $\{\mathbf{b}, \boldsymbol{\theta}\}$ which maximize

$$Q(\{\mathbf{b}, \theta\}) = \sum_{l=1}^{n} V_l(T_\theta(\bar{\mathbf{x}}_l + \mathbf{P}_l\mathbf{b} + \mathbf{r}_l)) \quad (1)$$

where $\bar{\mathbf{x}}_l$ is the mean position of the landmark in a suitable reference frame, $\mathbf{P}_l$ is a set of modes of variation, $\mathbf{b}$ are the shape model parameters, $\mathbf{r}_l$ allows small deviations from the model, and $T_{\boldsymbol{\theta}}$ applies a global transformation (e. g. similarity) with parameters $\boldsymbol{\theta}$.

3.2. Quantitative evaluation and analysis

For Challenge 1, all proposed methods are evaluated against the ground truth on 250 cephalometric X-ray images, including 150 Test1 images and 100 Test2 images.

(1) IEEE ISBI 2015 challenge.

Figs. 5 and6 present the overall results of MRE, SD and SDR using four precision ranges for the detection of the 19 anatomical landmarks. It is observed that Lindner and Cootes's method achieves the highest SDRs (73.68%, 80.21%, 85.19% and 91.47% in Test1 and 66.11%, 72%,77.63% and 87.42% in Test2 using 2 mm, 2.5 mm, 3 mm, and 4 mm precision ranges) and the lowest MRE and SD (1.67 mm and 1.48 mm in Test1 and 1.92 mm and 1.24 mm in Test2). Based on MRE, both methods are able to achieve MREs lower

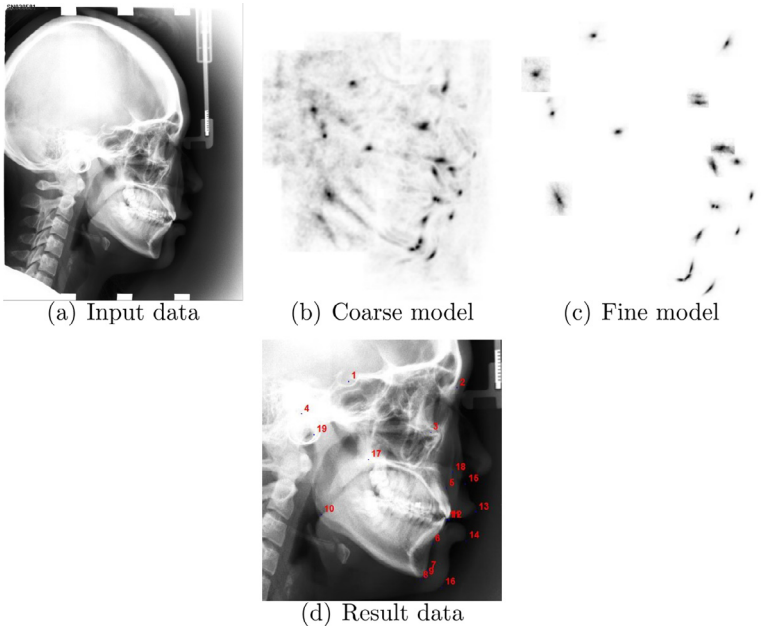

Fig. 4. Superposition of voting images for the 19-point RFRV-CLMs.

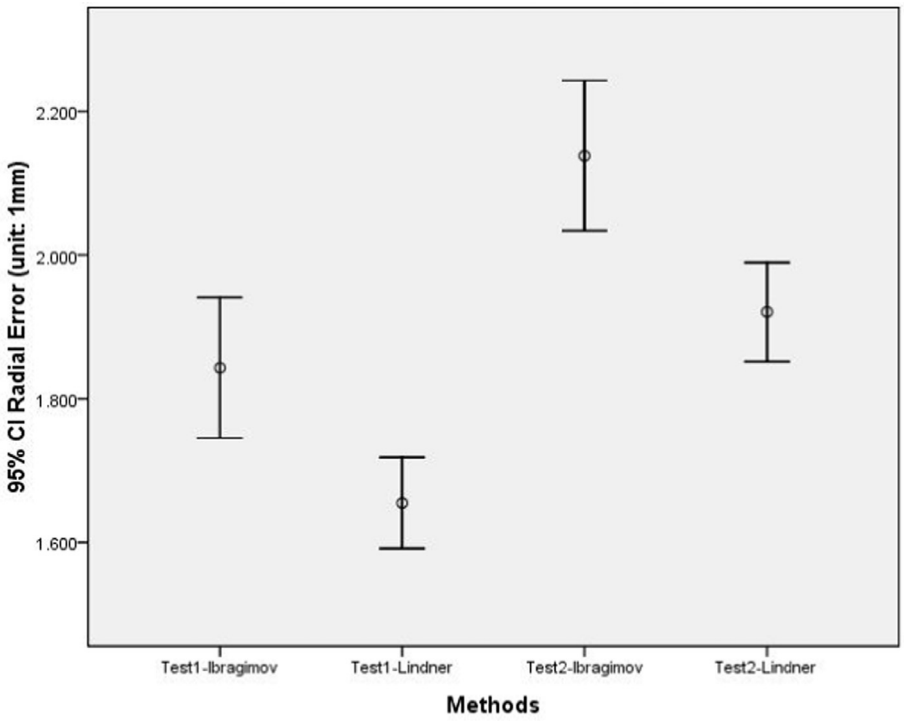

Fig. 5. Mean radial errors with error bar of two on-site competition methods.

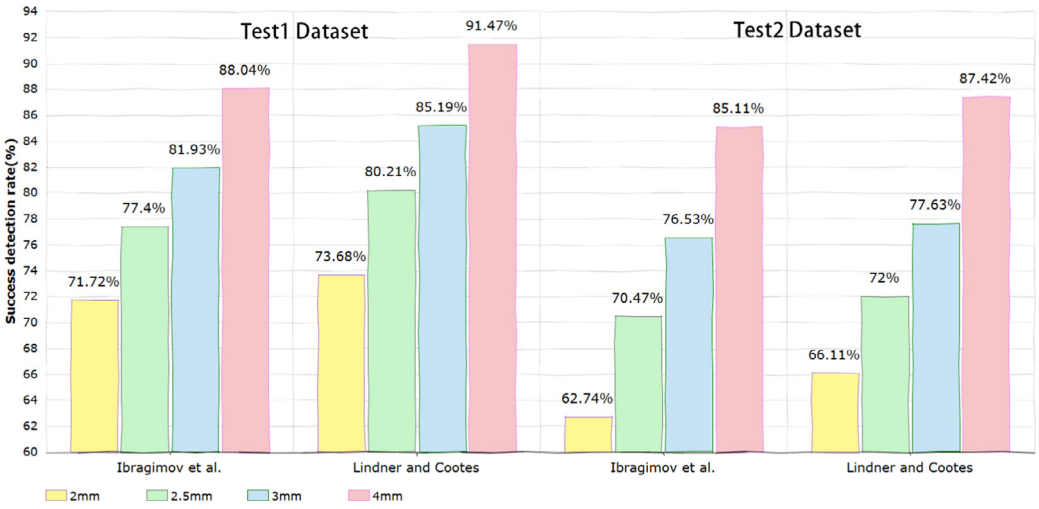

Fig. 6. Success detection rates (SDRs) using four precision ranges, including 2 mm (yellow), 2.5 mm (green), 3 mm (blue) and 4 mm (red), of two on-site competition methods. (For interpretation of the references to color in this figure legend, the reader is referred to the web version of this article.)

than 2.5 mm on Test1 and Test2, but only Lindner and Cootes's method obtains the MREs lower than 2.0 mm on both datasets. Table 4 presents the confusion matrices of the eight classifications of the anatomical types on Test1 dataset. The success classification rates of Ibragimov et al.'s method and Lindner and Cootes's method are 70.84% and 76.41%. Confusions among some classes are observed (e.g. Type 2 and Type 1 on ANB, Type 1 and Type 3 on ANB, Type 2 and Type 1 on SNA, Type 3 and Type 1 on ODI, and Type 2 and Type 1 on FHI). Table 5 shows the confusion matrices of the eight classification of the anatomical types on Test2 dataset. The success classification rates of Ibragimov et al.'s method and Lindner and Cootes's method are 76.12% and 80.99%. Confusions among some classes are observed (e.g. Type 2 and Type 1 on ANB, Type 1 and Type 3 on ANB, Type 2 and Type 1 on SNB, Type 1 and Type 3 on SNB, Type 2 and Type 1 on SNA, Type 2 and Type 1 on ODI, Type 1 and Type 3 on FHI, Type 1 and Type 2 on FHA, and Type 4 and Type 1 on MW).

(2) Compared with methods in IEEE ISBI 2014 Challenge

Figs. 7 and8 compare the overall results of MRE, SD and SDR using four precision ranges for the detection of the 19 anatomical landmarks between the five methods in the 2014 Challenge (Wang, 2015) and the two submitted methods in this 2015 Challenge on the same 100 images. It is observed that the two methods, submitted in 2015, are better than all the methods that were submitted in 2014. Lindner and Cootes's method achieves the highest SDRs (74.84%, 80.37%, 84.79%, and 89.95%) using 2 mm, 2.5 mm, 3 mm, and 4 mm precision ranges and the lowest MRE (1.656 mm) and SD

Table 4
Confusion matrices for the classifications of anatomical types on Test1 dataset. The success classification rates of method of Ibragimov et al. and Lindner and Cootess method are 70.84% and 76.41%.

Test1 dataset	Ibragimov et al.				Lindner and Cootes			
		Estimation				Estimation		
		Type1	Type2	Type3		Type1	Type2	Type3
Reference standard	ANB	Diagonal average: 59.42%			ANB	Diagonal average: 64.99%		
	Type1	46.15%	7.69%	**46.15%**	Type1	53.85%	7.69%	**38.46%**
	Type2	**48.57%**	40.00%	11.43%	Type2	**37.14%**	54.29%	8.57%
	Type3	5.26%	2.63%	92.11%	Type3	9.21%	3.95%	86.84%
Reference standard	SNB	Diagonal average: 71.09%			SNB	Diagonal average: 84.52%		
	Type1	71.43%	17.14%	11.43%	Type1	82.86%	8.57%	8.57%
	Type2	**41.67%**	58.33%	0.00%	Type2	16.67%	83.33%	0.00%
	Type3	14.56%	1.94%	83.50%	Type3	11.65%	0.97%	87.38%
Reference standard	SNA	Diagonal average: 59.00%			SNA	Diagonal average: 68.45%		
	Type1	47.50%	10.00%	**42.50%**	Type1	72.50%	12.50%	15.00%
	Type2	**37.35%**	55.42%	7.23%	Type2	**25.30%**	69.88%	4.82%
	Type3	18.52%	7.41%	74.07%	Type3	**29.63%**	7.41%	62.96%
Reference standard	ODI	Diagonal average: 78.04%			ODI	Diagonal average: 84.64%		
	Type1	77.42%	9.68%	12.90%	Type1	83.87%	9.68%	6.45%
	Type2	**20.00%**	80.00%	0.00%	Type2	6.67%	93.33%	0.00%
	Type3	**23.29%**	0.00%	76.71%	Type3	**21.92%**	1.37%	76.71%
Reference standard	APDI	Diagonal average: 80.16%			APDI	Diagonal average: 82.14%		
	Type1	75.00%	12.50%	12.50%	Type1	77.50%	17.50%	5.00%
	Type2	**26.32%**	71.05%	2.63%	Type2	13.16%	84.21%	2.63%
	Type3	5.56%	0.00%	94.44%	Type3	15.28%	0.00%	84.72%
Reference standard	FHI	Diagonal average: 58.97%			FHI	Diagonal average: 67.92%		
	Type1	68.29%	2.44%	**29.27%**	Type1	76.32%	1.32%	**22.37%**
	Type2	**83.33%**	16.67%	0.00%	Type2	**66.67%**	33.33%	0.00%
	Type3	8.06%	0.00%	91.94%	Type3	5.88%	0.00%	94.12%
Reference standard	FHA	Diagonal average: 77.03%			FHA	Diagonal average: 75.54%		
	Type1	60.98%	**29.27%**	9.76%	Type1	60.53%	**31.58%**	7.89%
	Type2	6.98%	91.86%	1.16%	Type2	5.81%	93.02%	1.16%
	Type3	13.04%	8.70%	78.26%	Type3	**23.08%**	3.85%	73.08%
Reference standard	MW	Diagonal average: 83.94%			MW	Diagonal average: 82.19%		
		Type1	Type3	Type4		Type1	Type3	Type4
	Type1	73.33%	11.11%	15.56%	Type1	75.56%	**20.00%**	4.44%
	Type3	12.90%	85.48%	1.61%	Type3	6.45%	91.94%	1.61%
	Type4	2.33%	4.56%	93.02%	Type4	18.60%	2.33%	79.07%

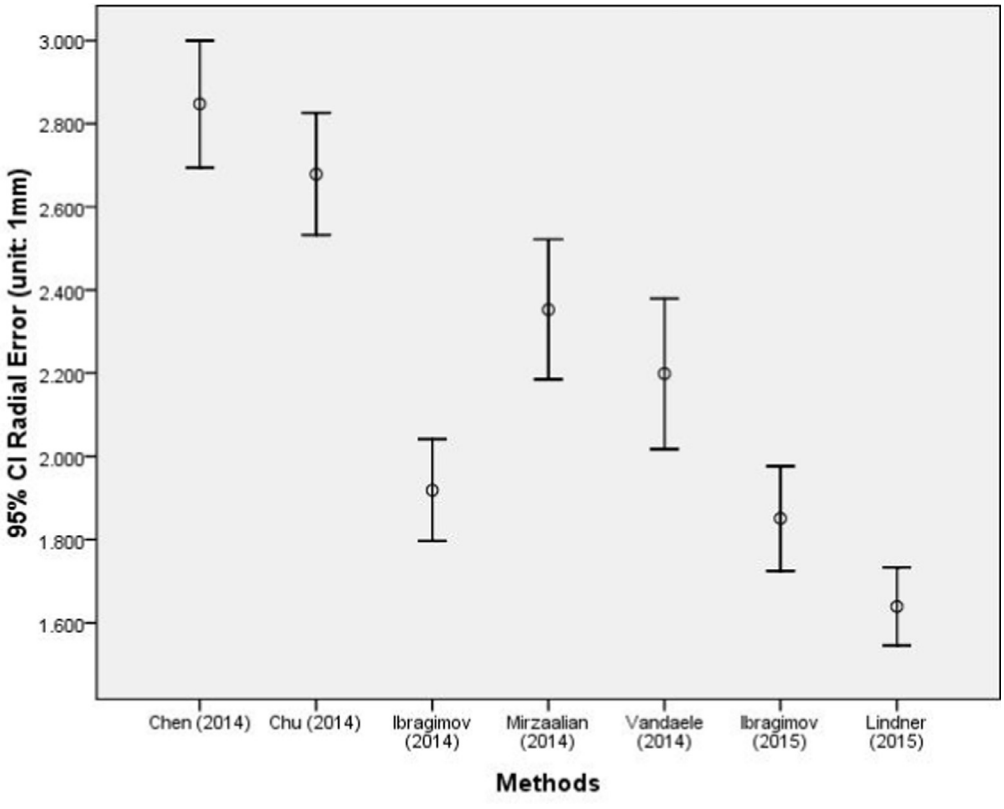

Fig. 7. Mean radial errors with error bar of five methods in 2014 and two methods in 2015 on same 100 images.

Table 5
Confusion matrices for the classifications of anatomical types on Test2 dataset. The success classifications rates of Ibragimov et al.s method and Lindner and Cootess method are 76.12% and 80.99%.

Test2 dataset	Ibragimov et al.				Lindner and Cootes			
		Estimation				Estimation		
		Type1	Type2	Type3		Type1	Type2	Type3
Reference standard	ANB	Diagonal Average: 76.64%			ANB	Diagonal Average: 75.83%		
	Type1	67.74%	0.00%	**32.26%**	Type1	64.52%	3.23%	**32.26%**
	Type2	**25.93%**	74.07%	0.00%	Type2	**33.33%**	62.96%	3.00%
	Type3	11.90%	0.00%	88.10%	Type3	0.00%	0.00%	100%
Reference standard	SNB	Diagonal Average: 75.24%			SNB	Diagonal Average: 81.92%		
	Type1	61.29%	12.90%	**25.81%**	Type1	74.19%	3.23%	**22.58%**
	Type2	**23.08%**	76.92%	0.00%	Type2	**23.08%**	76.92%	0.00%
	Type3	10.71%	1.79%	87.50%	Type3	3.57%	1.79%	94.64%
Reference standard	SNA	Diagonal Average: 70.24%			SNA	Diagonal Average: 77.97%		
	Type1	65.12%	18.60%	16.28%	Type1	79.07%	9.30%	11.63%
	Type2	**25.00%**	75.00%	0.00%	Type2	**25.00%**	72.50%	2.50%
	Type3	**23.53%**	5.88%	70.59%	Type3	17.65%	0.00%	82.35%
Reference standard	ODI	Diagonal Average: 63.71%			ODI	Diagonal Average: 71.26%		
	Type1	70.37%	7.41%	**22.22%**	Type1	81.48%	1.85%	16.67%
	Type2	**60.00%**	40.00%	0.00%	Type2	**60.00%**	40.00%	0.00%
	Type3	19.23%	0.00%	80.77%	Type3	7.69%	0.00%	92.31%
Reference standard	APDI	Diagonal Average: 79.93%			APDI	Diagonal Average: 87.25%		
	Type1	80.95%	11.90%	7.14%	Type1	80.95%	9.52%	9.52%
	Type2	**27.27%**	72.73%	0.00%	Type2	13.64%	86.36%	0.00%
	Type3	13.89%	0.00%	86.11%	Type3	5.56%	0.00%	94.44%
Reference standard	FHI	Diagonal Average: 86.74%			FHI	Diagonal Average: 90.90%		
	Type1	72.41%	1.72%	**25.86%**	Type1	77.59%	1.72%	**20.69%**
	Type2	0.00%	100%	0.00%	Type2	0.00%	100%	0.00%
	Type3	12.20%	0.00%	87.80%	Type3	4.88%	0.00%	95.12%
Reference standard	FHA	Diagonal Average: 78.90%			FHA	Diagonal Average: 80.66%		
	Type1	59.09%	**36.36%**	4.55%	Type1	72.73%	**22.73%**	4.55%
	Type2	**22.39%**	77.61%	0.00%	Type2	15.38%	84.62%	0.00%
	Type3	0.00%	0.00%	100%	Type3	15.38%	0.00%	84.62%
Reference standard	MW	Diagonal Average: 77.53%			MW	Diagonal Average: 82.11%		
		Type1	Type3	Type4		Type1	Type3	Type4
	Type1	82.93%	9.76%	7.32%	Type1	82.93%	4.88%	12.20%
	Type3	**23.08%**	76.92%	0.00%	Type3	15.38%	84.62%	0.00%
	Type4	**21.21%**	6.06%	72.73%	Type4	**21.21%**	0.00%	78.79%

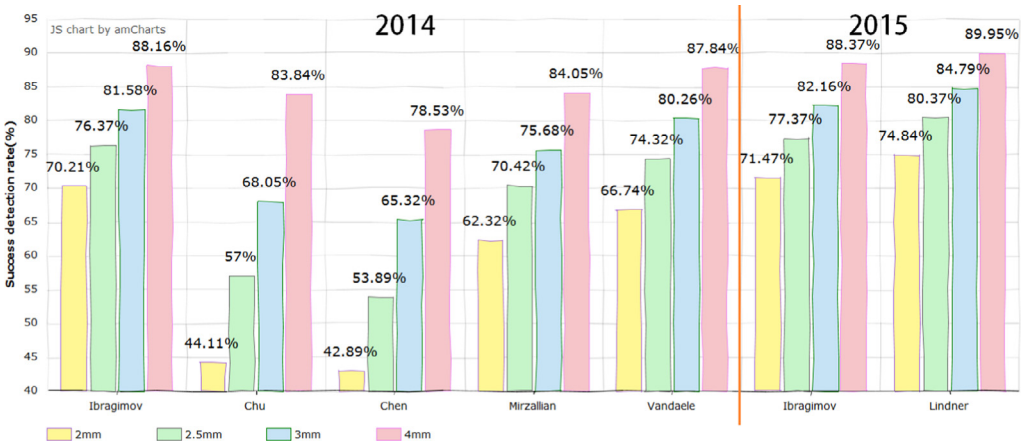

Fig. 8. Success detection rates (SDRs) using four precision ranges, including 2.0 mm (yellow), 2.5 mm (green), 3.0 mm (blue) and 4.0 mm (red), of five methods in 2014 and two methods in 2015 on same 100 images. (For interpretation of the references to color in this figure legend, the reader is referred to the web version of this article.)

(1.56 mm). Compared with the best method in 2014 (Ibragimov et al.(2014)), SDRs have increased about 4.4% on average (6.6% for 2 mm, 5.2% for 2.5 mm, 3.9% for 3 mm, and 2% for 4 mm) in 2015. However, the experimental results show that this is still an unsolved problem and needs further investigation as the highest SDR within 2mm precision range is only 74.84%.

Furthermore, to analyze the capabilities of methods in detection of individual landmarks, Fig. 9 compares the MRE values of the five 2014 methods and two 2015 methods on individual landmarks using the same 100 images. It is observed that the method of Lindner and Cootes generally performs best. Compared with the previous methods in 2014 (Wang, 2015), landmark 1, landmark 2, landmark 3, landmark 5, landmark 6, landmark 7, landmark 8, landmark 9, landmark 10, landmark 11, landmark 12, landmark 13, landmark 15, landmark 16, landmark 17 and landmark 18 are successfully detected with relatively low MREs by Lindner

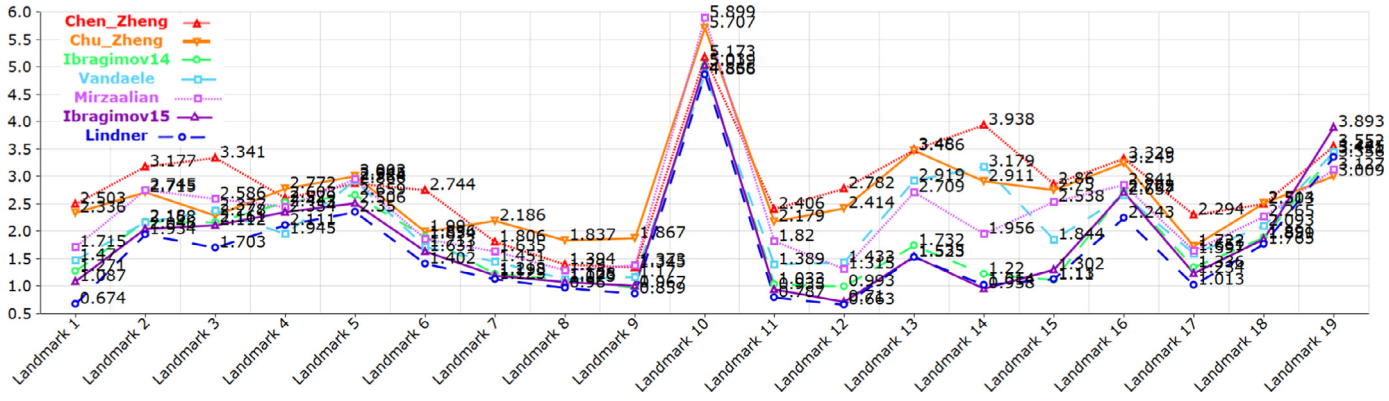

Fig. 9. Mean radial errors (unit: 1 mm) in detection of individual landmarks on the same 100 images. MREs in detection of L_{10} and L_{19} are particularly high, showing that these landmarks are especially difficult.

Table 6
Detection radial error (in mm) of 100 cephalometric X-ray images with ANOVA analysis.

Method	*N*	Mean	Std. deviation	Std. error
Chen (2014)	100	28.4722	7.69665	.76966
Chu (2014)	100	26.7896	7.39018	.73902
Ibragimov (2014)	100	19.1910	6.18062	.61806
Mirzaalian (2014)	100	23.5309	8.47840	.84784
Vandaele (2014)	100	21.9842	9.11095	.91110
Ibragimov	100	18.5070	6.35577	.63558
Lindner	100	16.5614	5.39071	.53907
ANOVA	df	Mean square	F	Sig.
Between groups	7	2080.937	41.738	<0.001
Within groups	792	49.857		
Total	799			

and Cootes's method. However, landmarks 10 and 19 are still difficult to detect. Table 6 presents the quantitative evaluation results on detection radial error (pixel) on 100 cephalometric X-ray images. In comparison, Lindner and Cootes's method achieves low averaged radial error (16.5614) while the other six methods obtain averaged radial errors ranging from 18.51 to 28.47. Using SPSS software, Table 7 shows the statistical analysis result of the paired sample T-test, showing that Lindner and Cootes's method is significantly better than the other methods ($p < 0.0001$).

(3) Computer specification and efficiency.
Ibragimov et al.: The landmark detection framework was implemented in C#, and executed on a personal computer with Intel Core i7 processor at 2.8 GHz, 8 GB of memory and Windows 7 operation system without graphics processing unit-assisted acceleration. Annotation of one cephalogram of size 1935 × 2400 pixels took on average 11.5 s.
Lindner and Cootes: The method was implemented in C++ using the VXL computer vision libraries. All experiments were performed in a VMware running Ubuntu 10.04 LTS with a single core CPU and 2 GB RAM. No parallel computing or GPU acceleration was used. When running the VMware on a 3.33-GHz Intel Core2Duo PC, the average runtime of the system to detect all 19 landmarks was less than 5 s per image.

(4) Analysis and discussion
Table 8 presents the comparison table between the five methods of the ISBI 2014 landmark detection challenge and the two methods of the ISBI 2015 landmark detection challenge, and Table 9 presents the ranks of each landmark with seven submitted methods in the 2014 and 2015 landmark detection challenges. Lindner and Cootes method achieves the 17 best detection results on 19 landmarks. Table 10 presents the success classification rates for the five 2014 methods and two 2015 methods. It is observed that some anatomical types are difficult to classify, e.g. ANB and FHI. The best success classification rates of ANB and FHI are lower than 70%. The reason why some anatomical types are difficult to classify is that landmarks, which are difficult to detect, are used in the classification tasks, e.g. the landmark 5 is used in ANB classification, and the landmark 10 is used in FHI classification. Overall, the two 2015 methods (Lindner and Cootes and Ibragimov et al.) perform better than the five 2014 approaches. Most methods are based on Random Forest (RF), which is an ensemble learning method that uses a combination of randomized decision trees to calculate a response. During training, the decision trees split the feature space to obtain a better representation of the data. Compared with the submitted methods in the ISBI 2014 challenge, the averaged accuracy and runtime of detecting landmarks are significantly improved by Lindner and Cootes' method in the ISBI 2015 challenge (MRE: 1.656 mm and runtime per image: < 5s, without the requirement for high-performance hardware). Furthermore, all their detectors are

Table 7
Paired sample T-test for Lindner and Coote's method and the other six methods in MRE.

	Mean	Std. dev.	*t*	df	Sig. (2-tailed)
Chen (2014) - Lindner	11.91	5.63	21.138	99	<0.0001[a]
Chu (2015) - Lindner	10.23	5.59	18.313	99	<0.0001[a]
Ibragimov (2014) - Lindner	2.63	4.56	5.769	99	<0.0001[a]
Mirzaalian (2014) - Lindner	6.97	6.96	10.017	99	<0.0001[a]
Vandaele (2014) - Lindner	5.42	7.21	7.519	99	<0.0001[a]
Ibragimov–Lindner	1.95	4.66	4.173	99	<0.0001[a]

[a] Lindner and Cootes's method is significantly better than other methods (p <0.0001).

Table 8
Comparison table for the seven accepted methods of the 2014 and 2015 automated landmark detection challenges.

Method (year)	Base method	Features	Average ranking (MRE value)
Chen and Zheng (2014)	Voting	•Sparse shape composition model •Voting strategy	7 (2.847)
Chu et al. (2014)	Random forest	•Landmark correction: sparse shape composition model	6 (2.679)
Ibragimov et al. (2014) (best method in 2014)	Random forest	•Haar-like features •Game theory •Spatial relationships among pairs of landmarks, modeled by Gaussian kernel density estimation.	3 (1.919)
Mirzaalian and Hamarneh (2014)	Random forest	•A pictorial structure algorithm with data likelihood and regularization energy terms.	5 (2.353)
Vandaele et al. (2014)	Extremely randomized trees	•Training pixels are randomly extracted in a radius of at most 4 cm to the landmark. •All method parameters are tuned via 10-fold cross-validation.	4 (2.198)
Ibragimov et al. (2015)	Random forest	•Pairwise spatial relationships among landmarks through the optimal assignment-based shape representation •Multi-landmark spatial relationships through the random forest-based representation •Haar-like appearance features •Game theory	2 (1.851)
Lindner and Cootes (2015) (best method in 2015)	Random forest	•Regression-voting •Constrained local model framework •Houghforests.	1 (1.656)

Table 9
The ranking of each landmark for the seven accepted methods in the 2014 and 2015 automated landmark detection challenges.

Method	L_1	L_2	L_3	L_4	L_5	L_6	L_7	L_8	L_9	L_{10}	L_{11}	L_{12}	L_{13}	L_{14}	L_{15}	L_{16}	L_{17}	L_{18}	L_{19}	#Rank1
Chen and Zheng	7	7	7	6	7	7	7	6	5	5	7	7	7	7	7	7	7	6	6	0/19
Chu et al.	6	5	4	7	4	6	6	7	7	6	6	6	6	6	6	6	6	7	1	1/19
14-Ibragimov et al.	3	4	3	5	3	5	3	3	3	3	3	3	3	3	3	4	3	3	4	0/19
Mirzaalian and Hamarneh	5	6	6	4	6	4	5	5	6	7	5	4	4	5	5	5	5	5	2	0/19
Vandaele et al.	4	3	5	1	5	3	4	4	4	2	4	5	5	4	4	2	4	4	5	1/19
15-Ibragimov et al.	2	2	2	3	2	2	2	2	2	4	2	2	2	2	2	3	2	2	7	0/19
Lindner and Cootes	1	1	1	2	1	1	1	1	1	1	1	1	1	1	1	1	1	1	3	17/19

Table 10
The success classification rates of the five 2014 methods and two 2015 methods the accepted methods.

	ANB (%)	SNB (%)	SNA (%)	ODI (%)	APDI (%)	FHI (%)	FHA (%)	MW (%)
Chen (2014)	51.04	63.73	48.69	66.18	64.86	54.14	62.55	60.98
Chu (2014)	48.00	70.76	51.49	73.17	65.94	50.88	67.31	60.16
Ibragimov (2014)	60.81	74.33	64.31	75.62	82.40	64.40	72.81	86.82
Mirzaalian (2014)	55.48	72.32	60.28	72.50	68.25	51.09	71.23	74.68
Vandaele (2014)	**63.48**	68.25	67.93	82.06	74.81	**67.02**	70.49	77.89
Ibragimov	60.89	72.80	66.95	85.90	**85.52**	61.19	**80.66**	**89.12**
Lindner	63.41	**84.40**	**73.27**	**93.20**	85.11	65.90	76.94	82.56

*The best methods for the anatomical type are marked in bold.

trained independently, which facilitates the inclusion of additional landmarks. On the contrary, this also means that their RF-voting for the best landmark position does not take inter-landmark relationships into account. However, their method utilizes statistical shape models (Cootes, 1995) to regularize the output of the individual predictions for each landmark. This combined with using Random Forests for regression rather than classification leads to significantly improved results. It is worth pointing out that, even though their system achieves high performance in the given challenges, the accuracy of this system relies on the shape and appearance of the object of interest exhibited in the training data. Hence, when training a landmark detection system based on their proposed RF-based approach, the training data needs to be representative for the unseen data to which the system is going to be applied. Furthermore, all presented landmark detection methods represent supervized learning and hence require a sufficient number of manually annotated training data.

Future developments to further improve the performance of automatic cephalometric landmark detection may include algorithms that are less reliant on the shape and appearance to be exhibited in the training data, and require significantly less (none) annotated training data.

4. Challenge 2: bitewing radiography analysis

4.1. Methods

(1) Ronneberger et al.
Ronneberger et al. present a pure machine learning approach using a u-shaped deep convolutional neural network ("u-net") for the fully automated segmentation of dental x-ray images. The architecture of the u-net consists of a

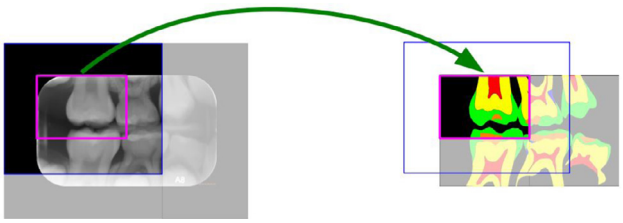

Fig. 10. Overlap-tile strategy for seamless segmentation of arbitrarily large images. Prediction of the segmentation in the magenta area, requires image data within the blue area as input. Missing input data is extrapolated by zero padding.

contracting path to capture context and a symmetric expanding path that enables precise localization. Such a network can be trained end-to-end from very few images. The network learns the desired robustness to deformations by augmenting the training data with randomly deformed images. One important modification in Ronneberger et al.'s architecture is that in the upsampling part we have also a large number of feature maps, which allows the network to propagate context information to higher resolution layers. As a consequence, the expansive path is more or less symmetric to the contracting path, and yields a u-shaped architecture. The network does not have any fully connected layers and only uses the valid part of each convolution, i.e., the segmentation map only contains the pixels, for which the full context is available in the input image. This strategy allows the seamless segmentation of arbitrarily large images by an overlap-tile strategy (see Fig. 10). To predict the pixels in the border region of the image, the missing context is extrapolated by zero padding. This tiling strategy is important to apply the network to large images, since otherwise the resolution would be limited by the GPU memory. The network architecture is illustrated in Fig. 11. It consists of a contracting path (left side) and an expansive path (right side). The contracting path follows the typical architecture of a convolutional network. It consists of the repeated application of two 3×3 convolutions (only using the valid part), each followed by a rectified linear unit (ReLU) and a 2×2 max pooling operation with stride 2 for downsampling. At each downsampling step we double the number of feature maps. Every step in the expansive path consists of a spatial upsampling of the feature maps with a factor of 2 followed by a 4×4 convolution that halves the number of feature maps, a concatenation with the correspondingly cropped feature maps from the contracting path, and one or two 3×3 convolutions, each followed by a ReLU. The cropping is necessary due to the loss of border pixels in every convolution. At the final layer a 1×1 convolution is used to map each 64-dim feature vector to the desired number of classes (here 7). In total the network has 23 convolutional layers. Further details are available in Ronneberger (2015) and Fig. 12 presents the results of Ronneberger et al.'s method.

(2) Lee et al.

In this work, Lee et al. built a random forest based dental segmentation system, which consists of a random forest machine learning system and a post-processing model for refining the prediction output *PD* based on the probability maps *PB*s generated by the machine learning system. 275 image features categorized in 24 types are extracted for training. The data is trained using random forest (Breiman, 2001) with 50 trees generated. The prediction output *PD* can be generated by following equation.

$$Combined\ PB(x,y) = \underset{i}{\operatorname{argmax}}\ PB_i(x,y), \tag{2}$$

where $i = 1$ to 7, x is X-coordinate and y is Y-coordinate. The second part is a a post-processing model. In order to refine the prediction outputs, two filters and morphological operations are applied in the combined probability map. First, two filters are 3×3 for removing single class and 5×5 for removing 3×3 classes. In a 3×3 four-neighbor rule, a position has only 4 neighboring classes that share a side. If 4 neighboring classes are same and the current class is different from 4 neighboring classes, the class of current position will be changed to the same class with 4 neighboring classes. In a 5×5 neighbor rule, if a isolated 3×3 block

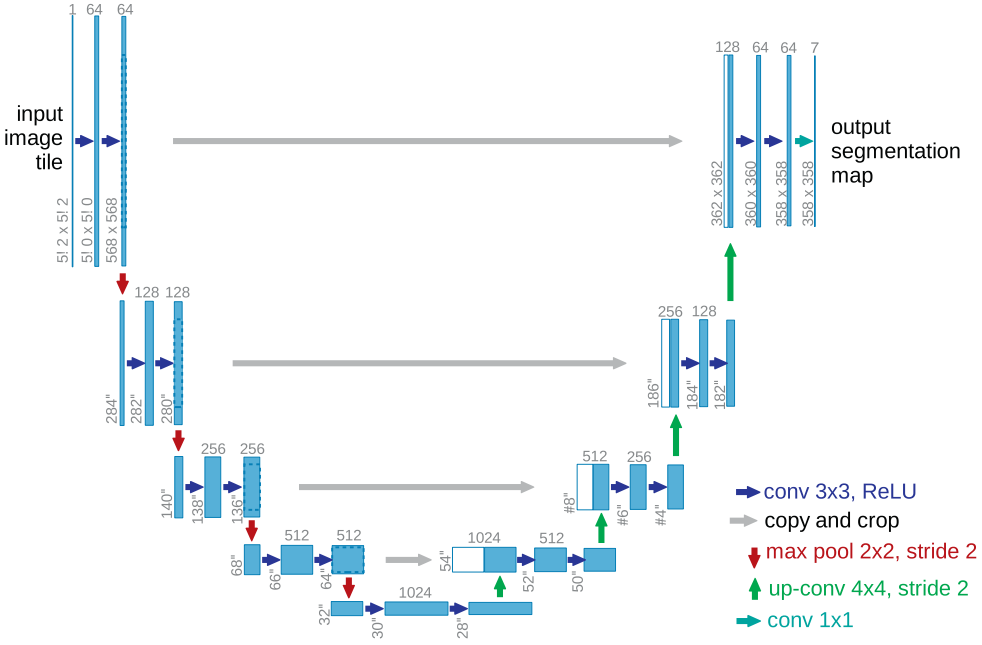

Fig. 11. U-net architecture (example for 32×32 pixels in the lowest resolution). Each blue box corresponds to a stack of feature maps. The number of features is denoted on top of the box. The x-y-size is provided at the lower left edge of the box. White boxes represent copied feature maps. The arrows denote the different operations.

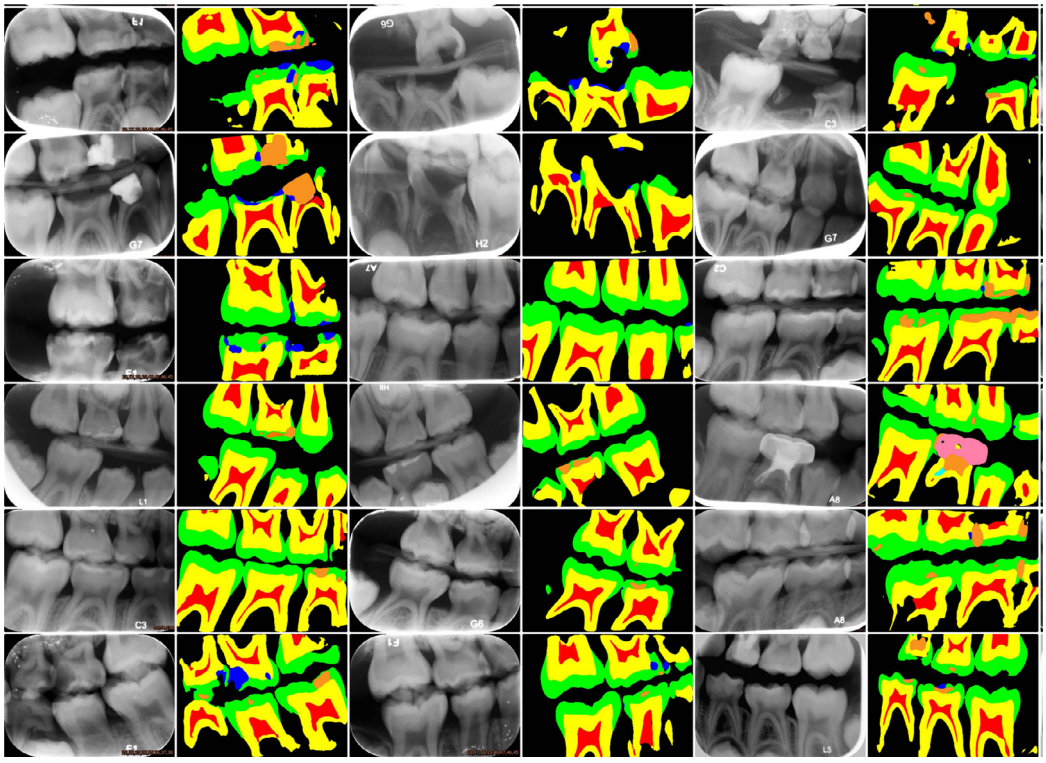

Fig. 12. Results of Ronneberger et al.'s method.

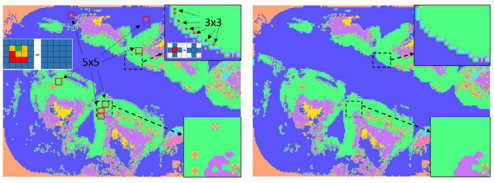

(a) The original combined probability map (b) The combined probability map after applying 3x3 and 5x5 filters

Fig. 13. Two filters were used on the probability map in Lee et al.'s method.

with same neighboring classes, all classes of the block will be changed to the same class with the neighboring classes. Fig. 13 shows that two filters were used on the probability map. Fig. 13(a) is the original combined probability map and Fig. 13(b) is the combined probability map after applying 3 × 3 and 5 × 5 filters. Second, the combined *PB* can be separated into seven binary prediction maps *PDs* by following equations.

$$\begin{cases} PD_i(x,y) = 1, & \text{if } Combined\ PB(x,y) \in i \quad (3) \\ 0, & \text{otherwise} \quad (4) \end{cases}$$

4.2. Quantitative evaluation and analysis

For Challenge 2, all proposed methods are evaluated against the ground truth on 80 bitewing X-ray images, including 40 Test1 images and 40 Test2 images.

(1) Quantitative evaluation
Table 11 presents the quantitative evaluation results for the segmentation of seven dental structures of the two submitted methods. The average precisions of Ronneberger et al.'s method and Lee et al.'s method are (0.455 and 0.226 in Test1, 0.419 and 0.195 in Test2), respectively. The best precisions for segmenting the enamel, dentin, pulp are 0.551, 0.674 and 0.598 in Test1 and 0.542, 0.66 and 0.613 in Test2, respectively. However, for detecting caries, both methods perform poor and obtain less than 1% precision. The averaged F-score values of Ronneberger et al.'s method and Lee et al.'s method are 0.567 and 0.322 in Test1 and 0.525 and 0.287 in Test2.

(2) Computer specification and efficiency
Ronneberger et al.: The network was implemented using the Caffe-Framework (Jia, 2014), which is written in C++ and CUDA for the GPU parts. The augmentation and the tiled execution are implemented in Matlab. The whole training process of one network took about 10 hours on a NVidia Titan GPU. The execution time is approx. 1.5 sec per image on a Laptop which was used at the on-site competition (Core i7 CPU, 32 GB RAM, NVidia GTX980m GPU with 8 GB of RAM).
Lee et al.: The algorithm was implemented in Java. In training phase, all experiments was implemented in a computer with two Intel Xeon E5-2650 processors at both 2.00 GHz, 128 GB of DDR3 memory and Windows 7 operation system, and the training phase took about 3.38 hours. In testing step, all experiments was implemented in a computer with two Intel Xeon E5-2687 processors at both 3.1 GHz, 16 GB of DDR3 memory and Windows 7 operation system. The average execute time is less than 2.5 minutes per bitewing X-ray image.

(3) Analysis and discussion
Segmentation of dental structures in bitewing radiographs is difficult as the data variation is high and teeth are sometimes labeled as background (see Fig. 14), which makes the learning task difficult. There are nine teams registered to this challenge, but only two teams successfully submitted the test results. The averaged F-scores of the teams

Table 11
Quantitative evaluation of tooth structure segmentation algorithms on bitewing radiographs.

Test 1 dataset	Precision		Sensitivity		Specificity		F-score	
Types	Ronneberger et al.	Lee et al.	Ronneberger et al.	Lee et al.	Ronneberger et al.	Lee et al.	Ronneberger et al.	Lee et al.
Caries	0.073	0.022	0.12	0.06	0.998	0.989	0.119	0.042
Enamel	0.551	0.322	0.685	0.8	0.963	0.746	0.702	0.48
Dentin	0.674	0.48	0.782	0.75	0.936	0.766	0.801	0.642
Pulp	0.598	0.345	0.683	0.573	0.987	0.939	0.74	0.506
Crown	0.295	0.001	0.906	0.024	1	0.982	0.313	0.002
Restoration	0.403	0.241	0.547	0.521	0.996	0.966	0.515	0.349
Root canal treatment	0.179	0.045	0.179	0.144	1	0.999	0.266	0.068
Average	0.455	0.226	0.578	0.548	0.983	0.912	0.567	0.322
Test 2 dataset								
Caries	0.078	0.032	0.086	0.05	0.999	0.991	0.131	0.061
Enamel	0.542	0.291	0.736	0.787	0.956	0.753	0.689	0.44
Dentin	0.66	0.44	0.799	0.754	0.933	0.756	0.784	0.601
Pulp	0.613	0.319	0.699	0.608	0.992	0.932	0.748	0.473
Crown	0.295	0.02	0.459	0.205	1	0.99	0.353	0.032
Restoration	0.26	0.145	0.443	0.392	0.992	0.967	0.342	0.23
Root canal treatment	0.098	0.027	0.099	0.058	1	1	0.157	0.045
Average	0.419	0.195	0.531	0.497	0.982	0.913	0.525	0.287

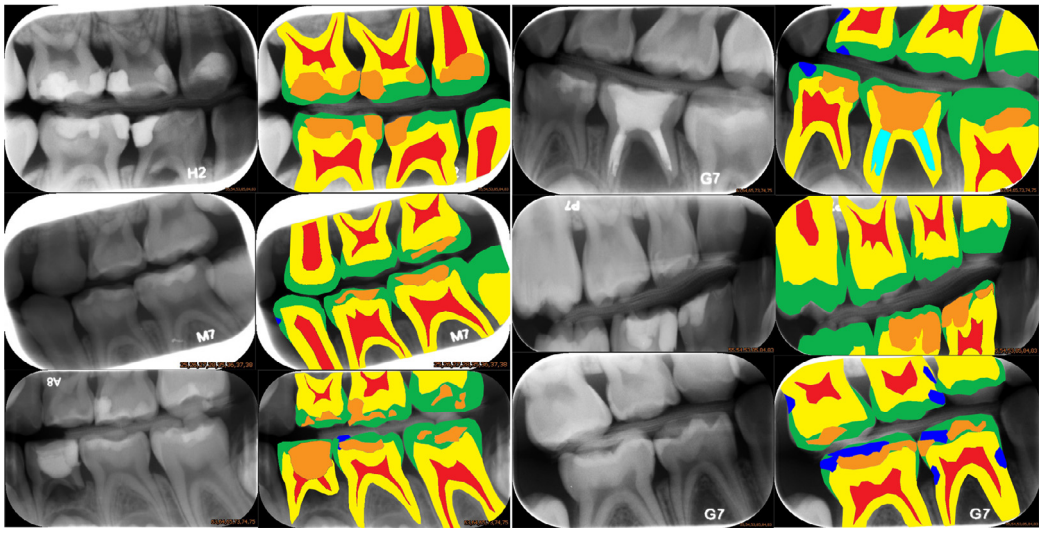

Fig. 14. Six samples of seven dental structures in bitewing radiography with raw image (left side) and manual segmentation result (right side).

(Ronneberger et al. and Lee et al.) are 0.560 and 0.268, respectively, and the u-shaped deep convolutional network by Ronneberger et al. performs significantly better and achieves F-scores greater than 0.7 for the three fundamental dental structures (*enamel, dentin* and *pulp*). The main advantage of the u-net architecture for this task is its ability to automatically learn the hierarchical structure within the images. During segmentation it uses the extracted context at all detail levels for the decision at each pixel. A critical part of Ronneberger et al.'s approach is data augmentation. As there is limited data available, Ronneberger et al. use data augmentation by applying elastic deformations to produce a large database with 20000 training image tiles, which is essential for machine learning methods to learn invariance and produce robust models. The value of data augmentation for learning invariance has also been shown in Dosovitskiy et al. (Dosovitskiy, 2014) in the scope of unsupervised feature learning. In the experiments, it is observed that the data augmentation technique helps to create reasonable additional training instances for enamel, dentin and pulp, but the other classes caries, crown, restoration and root canal treatment, appear quite different according to their relative location, so the augmentation is less successful here.

5. Conclusion

Computerized automatic dental radiography analysis systems for clinical use save time and manual costs and avoid problems caused by intra- and inter-observer variations e.g. due to fatigue, stress or different levels of experience. In this article, we have presented benchmarks for a number of challenging tasks in dental X-ray image analysis, including algorithms for (i) anatomical landmark detection on lateral cephalometric radiographs, (ii) anatomical abnormality classification on lateral cephalometric radiographs, and (iii) dental structure segmentation on bitewing radiographs. The presented results will allow the objective comparison of existing and new developments in the field. All methods were evaluated using a common lateral cephalometric radiography dataset repository, a common bitewing radiography dataset repository, ground truth data, and unified measurements for assessment of the detection, classification and segmentation accuracy. Based on the presented results, we can conclude that recent methods achieved significantly improved performance on these challenging tasks. However, the presented results also demonstrate that accurately analyzing dental radiographs remains a challenging problem which is still far from being solved. It is expected that this benchmark will help algorithmic developments, and that more advanced

approaches will be built and tested using the provided data repositories and benchmarks.

Acknowledgment

This work was supported by Tri-Service General Hospital-National Taiwan University of Science and Technology (TSGH-NTUST-C104011008 and C103008), Taiwan Ministry of Science and Technology (MOST1042221E011085) and Cardinal Tien Hospital (CTH10212C02). Ibragimov et al. was supported by the Slovenian Research Agency (P2-0232, L2-4072, J2-5473 and J7-6781). C. Lindner is funded by the Engineering and Physical Sciences Research Council, UK (EP/M012611/1). Ronneberger et al. was supported by the Excellence Initiative of the German Federal and State governments (EXC294) and by the BMBF (Fkz0316185B).

References

Breiman, L., 2001. Random forests. Mach. Learn. 45, 5–32.
Cootes, T., 1995. Active shape models - their training and application. Comput. Vis. Image Und. 61, 38–59.
Dosovitskiy, A., 2014. Discriminative unsupervised feature learning with convolutional neural networks. In: NIPS.
Downs, W.B., 1948. Variations in facial relationship, their significance in treatment and prognosis. Am. J. Orthod. 34 (10), 812–840.
Gayathri, V., Menon, H.P., 2014. Challenges in edge extraction of dental x-ray images using image processing algorithms - a review. Int. J. Comput. Sci. Inf. Technol. 5, 5355–5358.
Huh, J., 2015. Studies of automatic dental cavity detection system as an auxiliary tool for diagnosis of dental caries in digital x-ray image. Progr. Med. Phys. 25, 52–58.
Ibragimov, B., 2012. A game-theoretic framework for landmark-based image segmentation. IEEE Trans. Med. Imag. 31 (9), 1761–1776.
Ibragimov, B., 2014. Shape representation for efficient landmark-based segmentation in 3d. IEEE Trans. Med. Imag. 33 (4), 861–874.
Ibragimov, B., 2015. Segmentation of tongue muscles from super-resolution magnetic resonance images. Med. Image Anal. 20 (1), 198–207.
Jain, A.K., Chen, H., 2004. Matching of dental x-ray images for human identification. Pattern Recognit. 37, 1519–1532.
Jia, Y., 2014. Caffe: convolutional architecture for fast feature embedding. Proc. ACM Int. Conf. Multimed. 675–678.
Kim, Y.H., 1974. Overbite depth indicator: with particular reference to anterior openbite. Am. J. Orthod. 65 (6), 586–611.
Kim, Y.H., Vietas, J.J., 1978. Anteroposterior dysplasia indicator: an adjunct to cephalometric differential diagnosis. Am. J. Orthod. 73 (6), 619–633.
Kumar, 2011. Extraoral periapical radiography: an alternative approach to intraoral periapical radiography. Imag. Sci. Dent. 41, 161–165.
Lai, Y.H., Lin, P.L., 2008. Effective segmentation for dental x-ray images using texture-based fuzzy inference system. Adv. Concepts Intell. Vis. Syst. Lect. Notes Comput. Sci. 5259, 936–947.
Lin, P.L., 2010. An effective classification and numbering system for dental bitewing radiographs using teeth region and contour information. Pattern Recognit. 43, 1380–1392.
Lindner, C., et al., 2013. Fully automatic segmentation of the proximal femur using random forest regression voting. IEEE Trans. Med. Imag. 32, 1462–1472.
Lindner, C., et al., 2015. Robust and accurate shape model matching using random forest regression-voting. IEEE Trans. Pattern Anal. Mach. Intell. 37, 1862–1874.
Lpez-Lpez, J., 2012. Computer-aided system for morphometric mandibular index computation (using dental panoramic radiographs). Med. Oral Patol. Oral 17, e624–e632.
McNamara, J.J., 1984. A method of cephalometric evaluation. Am. J. Orthod. 86 (6), 449–469.
Nakamoto, T., 2008. A computer-aided diagnosis system to screen for osteoporosis using dental panoramic radiographs. Dentomaxillofacial Radiol. 37, 274–281.
Nanda, R., Nanda, R.S., 1969. Cephalometric study of the dentofacial complex of north indians. Angl. Orthod. 39 (1), 22–28.
Nikneshan, S., 2015. The effect of emboss enhancement on reliability of landmark identification in digital lateral cephalometric images. Iran. J. Radiol. 12, e19302.
Oliveira, J., Proenc, H., 2011. Caries detection in panoramic dental x-ray images. Comput. Vis. Med. Image Process.: Recent Trends, Comput. Meth. Appl. Sci. 19, 175–190.
Rad, A.E., 2013. Digital dental X-ray image segmentation and feature extraction. TELKOMNIKA 11, 3109–3114.
Ricketts, R.M., et al., 1982. Orthodontic Diagnosis and Planning, I and II. Rocky Mountain Orthod, Denver.
Ronneberger, O., 2015. U-net: Convolutional networks for biomedical image segmentation. In: Medical Image Computing and Computer-Assisted Intervention (MICCAI).accepted, url = http://arxiv.org/abs/1505.04597.
Sassouni, V., 1955. A roentgenographic cephalometric analysis of cephalo-facio-dental relationships. Am. J. Orthod. 41, 735–764.1955
Steiner, C.C., 1953. Cephalometrics for you and me. Am. J. Orthod. 39 (10), 729–755.
Tweed, C., 1946. The frankfort-mandibular plane angle in orthodontic diagnosis, classification, treatment planning, and prognosis. Am. J. Orthod. Oral Surg. 32 (1), 175–230.
Tweed, C.H., 1954. The frankfort mandibular incisal angle (FMIA) in orthodontic diagnosis, treatment planning, and prognosis. Angl. Orthod. 24, 121–169.
Viola, P., Jones, M., 2001. Rapid object detection using a boosted cascade of simple features. In: Proceedings CVPR 2001, pp. 511–518.
Wang, C.W., 2015. Evaluation and comparison of anatomical landmark detection methods for cephalometric X-ray images: A grand challenge. IEEE Trans. Med. Imag. 34 (9), 1–11.
Wenzel, A., 2001. Computer-automated caries detection in digital bitewings: consistency of a program and its influence on observer agreement. Caries Res. 35 (1), 12–20.
Wenzel, A., et al., 2002. Accuracy of computer-automated caries detection in digital radiographs compared with human observers. Eur. J. Oral Sci. 110 (3), 199–203.
Wriedt, S., 2012. Impacted upper canines: examination and treatment proposal based on 3d versus 2d diagnosis. J. Orofac. Orthop. 73, 28–40.
Zhou, J., Abdel-Mottaleb, M., 2005. A content-based system for human identification based on bitewing dental X-ray images. Pattern Recognit. 38, 2132–2142.